Z. Angew. Math. Phys. (2026) 77:180
© 2026 The Author(s)
0044-2275/26/060001-16
published online June 2, 2026
https://doi.org/10.1007/s00033-026-02826-5

Zeitschrift für angewandte Mathematik und Physik ZAMP

Chaotic dynamics of oscillators with combined elastic and dry friction nonlinearities

Vladimir Bratov and Sergey V. Kuznetsov

Abstract. The forced harmonic oscillator with combined Duffing cubic stiffness and Bliman–Sorine friction is analyzed using Poincaré sections and parameter space basins of attraction, constructed as functions of two key oscillator parameters: friction stiffness and forcing amplitude. The analysis uncovers several key dynamical features: (1) Chaotic behavior is absent when the cubic stiffness term vanishes; (2) chaotic regimes emerge as soon as the cubic stiffness becomes nonzero; (3) the parameter space develops strongly entangled basins, reflecting extreme sensitivity of attractor selection to frictional micro-mechanics; and (4) variations in the Bliman–Sorine parameters induce pronounced topological changes in bifurcation diagrams. These findings provide new insight into the structure of oscillations in systems governed by the Bliman–Sorine friction model. Numerical simulations are performed using a variable-step Adams–Bashforth–Moulton explicit–implicit scheme to ensure reliable long-time integration.

Mathematics Subject Classification. 74H60.

Keywords. Duffing oscillator, Bliman–Sorine friction model, Fractal dimension, Chaos, Basins of attraction, Bifurcation diagram.

1. Introduction

1.1. HDRB models

High-density rubber bearings (HDRB) exhibit strong geometric and material nonlinearities under moderate and large shear deformations. Experimental and theoretical studies show that the restoring force departs from linear elasticity due to hyperelastic behavior of rubber layers and geometric stiffening of laminated elastomeric structures [39,41]. A cubic stiffness term provides the leading-order correction to this nonlinear shear response and is widely used in various models of elastomeric isolators [52]. In addition to nonlinear elasticity, rubber bearings display pronounced hysteretic energy dissipation arising from micro-slip between rubber and steel shims, filler–matrix interactions in carbon-black-filled rubber, and partial slip at the bearing–foundation interface [8,16,40,73]; see Fig. 1.

These mechanisms generate smooth, rate-dependent hysteresis loops that cannot be adequately captured by models with a nonlinear spring and viscous damping, nor augmented models with Coulomb friction [35,46,49,61,63,71,75]. Dynamic friction and hysteresis models such as Dahl model [5,17,18,20,38,77], Armstrong–Hélouvîy model [3,13,65], Bliman–Sorine model [6,7,32,59], LuGre model [37,56,57], Brown–McPhee [12,14], and Bouc–Wen model [10,34,74] are introduced to reproduce pre-sliding displacement, memory effects, and amplitude-dependent dissipation characteristic of elastomeric bearings [1,2,11,23,27,55,72].

Among these formulations, the Bliman–Sorine friction formulation offers several important advantages over other friction models, particularly in the context of nonlinear dynamics. Unlike more empirical formulations, it is constructed as a mathematically well-posed hysteresis operator, which guarantees existence and uniqueness of solutions and ensures a clear dissipative structure [45,52,54]. This avoids non-physical

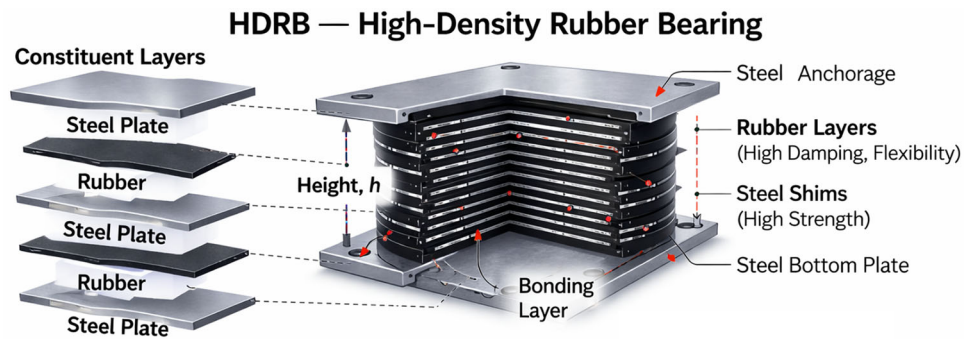


FIG. 1. Typical high-density rubber bearing (HDRB)

behaviors such as artificial energy generation or drift that may arise in Bouc–Wen or LuGre models if parameters are not carefully constrained. Moreover, with only two tuning parameters, the Bliman–Sorine model offers a physically simpler alternative to the multi-parameter Bouc–Wen formulation. Compared to Dahl's model, which is relatively simple and mainly suited for pre-sliding behavior, the Bliman–Sorine approach captures richer hysteretic effects while preserving analytical tractability. In contrast with the LuGre model, it does not rely on artificial bristle dynamics, which can introduce stiffness or spurious unphysical oscillations in simulations. Overall, the Bliman–Sorine formulation provides a balanced combination of physical consistency, mathematical rigor, and suitability for bifurcation and stability analysis, making it particularly attractive for studying nonlinear oscillatory systems.

Coupling a Duffing-type nonlinear spring with a Bliman–Sorine friction law provides a physically grounded and mathematically compact representation of the dominant nonlinearities—nonlinear stiffness and hysteretic dissipation—observed in HDRB used in seismic isolation and vibration mitigation [16,26,50,52,60].

1.2. Governing equations

The equation of motion for a Duffing-type oscillator with cubic nonlinearity [29,42,53] and the Bliman–Sorine friction law can be written in dimensionless form suggested in [67]:

$$\partial_\tau v = -\eta v - kx - \beta x^3 - F(v) + f\cos(\tau), \tag{1.1}$$

where $v = \partial_\tau x$; η is the linear dimensionless damping ratio; $k = 1$ is the normalized linear stiffness; β is the cubic stiffness coefficient; F is the friction force; f is the dimensionless driving force amplitude; and τ is the dimensionless time. The Bliman–Sorine friction law reads as

$$\partial_x F = \sigma \times \operatorname{sgn}\left(1 - \frac{F}{F_c}\operatorname{sgn}(v)\right) \times \left|1 - \frac{F}{F_c}\operatorname{sgn}(v)\right|^n, \tag{1.2}$$

where $n > 0$ is the nonlinearity exponent controlling the sharpness of the transition to saturation; σ is the dimensionless friction stiffness coefficient; and F_c denotes the dimensionless Coulomb sliding friction force. It should be noted that although Eq. (1.2) is known as the Bliman–Sorine model, it was originally introduced in [18].

The sign functions in Eq. (1.2) ensure directional consistency, while the absolute value term modulates the rate of change depending on how close the internal force F is to its saturation limit F_c. Physically, this model captures the gradual build-up of friction force during pre-sliding, the saturation at full slip, and the memory of previous loading direction. Unlike Coulomb friction, which switches abruptly, the

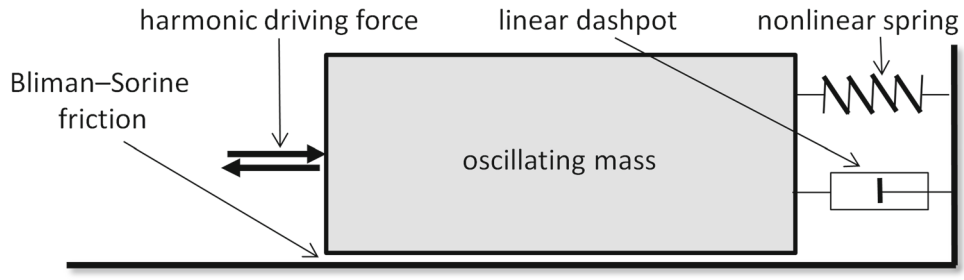


FIG. 2. Mathematical model for the Duffing-type oscillator with friction

Bliman–Sorine law produces smooth hysteresis loops and allows for continuous transitions between sticking and slipping regimes. This makes it especially useful in systems where friction interacts with nonlinear elasticity, such as rubber bearings. Coupled Eqs. (1.1) and (1.2) are used in the subsequent analysis.

More elaborate friction formulations—such as the full Armstrong–Hélouvîy, LuGre, Brown–McPhee, and Bouc–Wen models—are not considered here. Although they offer richer phenomenology, they also introduce substantially more tunable physical parameters (typically 4 in the Brown–McPhee model, 5–7 in the Armstrong–Hélouvîy model, and 6–8+ in both the LuGre and Bouc–Wen models). This higher dimensionality makes them less suitable for exploration of the parameter space undertaken in this study.

1.3. Problem statement

In this study, the Duffing-type forced harmonic oscillator containing a linear viscous damper, a cubic nonlinear spring, and a dry friction (Bliman–Sorine) element (Fig. 2) is analyzed.

The inclusion of the friction element in the Duffing oscillator is motivated by the fact that widely used seismic and vibration isolation systems exhibit various interfacial slip mechanisms that cannot be adequately represented by purely viscous damping. These mechanisms include micro-slip between rubber layers and steel shims in laminated bearings, filler–matrix interactions in carbon-black-filled rubber, and partial slip at the bearing–foundation interface. Such interfacial phenomena give rise to hysteretic energy dissipation, amplitude-dependent stiffness, and damping characteristics, which are more appropriately modeled through the addition of a dry friction component. Thus, the augmented Duffing oscillator provides a more realistic phenomenological representation of the nonlinear and dissipative behavior observed in practical elastomeric isolation systems.

The proposed model reveals a broad spectrum of dynamical phenomena that have not been studied in this context. In particular, it enables: (i) a systematic characterization of periodic, quasi-periodic, and chaotic regimes in the varying parameter space $(f, \omega, s, F_c, \beta, n)$; (ii) the identification and mapping of basins of attraction, including the detection of attractors that are remote from chaotic basins, which is of particular importance for the operational safety and reliability of high-damping rubber bearings (HDRBs); (iii) the analysis of multistability and coexistence of attractors, demonstrating the sensitivity of long-term system response to initial conditions and parameter perturbations; and (iv) the investigation of friction-induced bifurcations, grazing phenomena, and sudden transitions to chaos associated with stick–slip dynamic.

The analysis comprises two complementary diagnostic approaches: (I) Poincaré sections and bifurcation diagrams, which reveal the qualitative nature of the attractors and the transitions between periodic, quasi-periodic, and chaotic regimes; and (II) parameter space basins of attraction quantified using the cardinal number measure (CNM), which provides a systematic assessment of multistability and the relative prevalence of coexisting attractors [19,28,30]. To achieve reliable long-time integration of the essentially

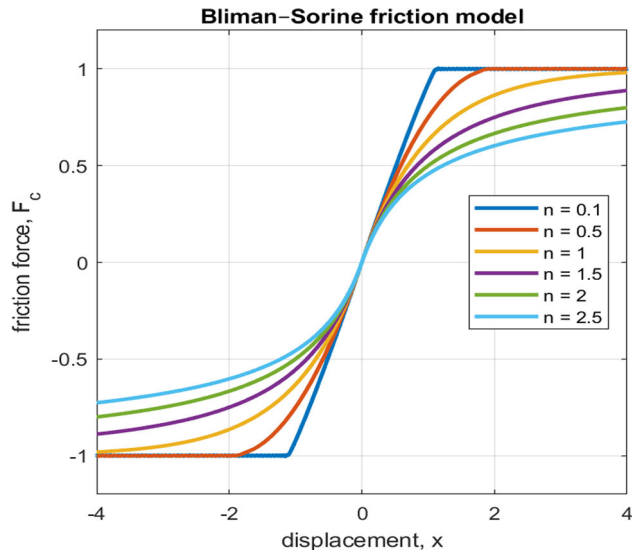


FIG. 3. Friction force versus displacement for Bliman–Sorine model

non-smooth system containing Bliman–Sorine friction model, numerical simulations are performed using a variable-step Adams–Bashforth–Moulton (ABM) explicit–implicit method [9,31,36,51,66], which is better suited than the Runge–Kutta solvers [4,58,62,78] and provides enhanced numerical stability and accuracy, which are essential for resolving the intricate dynamics generated by the considered Duffing-type oscillator with friction.

2. Principal equations

2.1. Friction force versus displacement

Integrating Eqs. (1.2) normalized at $\sigma = F_c = 1$; $v = \pm 1$ with different exponent n-values yields the following plots of friction force F versus displacement x (Fig. 3).

The curves in Fig. 3 illustrate the model's characteristic S-shaped hysteresis behavior, symmetric about the origin, with the friction force asymptotically approaching the normalized Coulomb levels $\pm F_s$ as the absolute displacement $|x|$ increases.

For small values of exponent $n < 1$, the transition from the pre-sliding regime to steady sliding is sharp. This behavior resembles classical Coulomb friction, but with pre-sliding compliance. As n increases to intermediate values ($n = 1$), the transition becomes noticeably smoother and more rounded, consistent with the classical Dahl-like response. A finite pre-sliding displacement is now more pronounced before the force approaches the asymptotic Coulomb value, reflecting greater compliance in the contact interface during the initial stages of motion. For larger exponents ($n \geq 1.5$), the pre-sliding region extends further and the curves exhibit a progressively gentler approach toward the sliding plateau. These results demonstrate that the exponent n serves as a single, effective tuning parameter that controls the nonlinearity and sharpness of the stick-to-slip transition in the Bliman–Sorine model. This flexibility makes the model particularly useful for qualitative studies of hysteresis-dominated systems and for exploring the sensitivity of system dynamics to variations in contact compliance, even in the absence of explicit velocity dependence.

2.2. Equations of motion

2.2.1. Non-autonomous system. Introducing a three-vector

$$X = \begin{pmatrix} x \\ v \\ w \end{pmatrix}, \tag{2.1}$$

where w satisfies the following equation derived from (1.2); see also [6,7]:

$$\partial_\tau w = a(v, w). \tag{2.2}$$

Herein,

$$a(v, w) = \sigma v \times \operatorname{sgn}\left(1 - \frac{w}{F_c}\operatorname{sgn}(v)\right) \times \left|1 - \frac{w}{F_c}\operatorname{sgn}(v)\right|^n \tag{2.3}$$

Equations (1.1), (1.2), and (2.2) are rewritten as an equivalent non-autonomous system of three coupled first-order equations [44]:

$$\partial_\tau X = G(X, \tau), \tag{2.4}$$

where

$$G(X, \tau) = \begin{pmatrix} v \\ -x - \beta x^3 - \eta v - w + f\cos(\tau) \\ a(v, w) \end{pmatrix}. \tag{2.5}$$

2.2.2. Autonomous system. To analyze the eigenvalues of the Jacobian matrix, it is necessary to transform the original non-autonomous system (2.4) into an autonomous form [33]. By introducing a new variable

$$\theta = \cos(\tau), \tag{2.6}$$

the desired autonomous system becomes

$$\partial_\tau Y = H(Y), \tag{2.7}$$

where

$$Y = \begin{pmatrix} x \\ v \\ w \\ \theta \end{pmatrix}; \qquad H(Y) = \begin{pmatrix} v \\ -x - \beta x^3 - \eta v - w + f\theta \\ a(v, w) \\ \pm\sqrt{1 - \theta^2} \end{pmatrix}. \tag{2.8}$$

2.3. Jacobian matrix and stiffness analysis

Taking the gradient of $H(Y)$ gives the Jacobian matrix:

$$J(Y) = \nabla_Y H(Y) = \begin{pmatrix} 0 & 1 & 0 & 0 \\ -1 - 3\beta x^2 & -\eta & -1 & \mp f\sqrt{1 - \theta^2} \\ 0 & \partial_v a(v, w) & \partial_w a(v, w) & 0 \\ 0 & 0 & 0 & \mp\frac{\theta}{\sqrt{1-\theta^2}} \end{pmatrix}. \tag{2.9}$$

Direct verification shows that one of the eigenvalues tends to zero for $\theta \to 0$ or $\theta \to \pm 1$, indicating the presence of a degenerate slow manifold in the considered dynamical system. The vanishing eigenvalue does not by itself prove stiffness in the strict numerical sense; however, it indicates the emergence of slow dynamics coexisting with faster decaying modes, which may produce stiff-like behavior and impose severe

constraints on explicit integration schemes, particularly near the degenerate states. According to [31], the stiffness ratio r can be defined as

$$r = \max_{i \neq j} \left| \frac{\mathrm{Re}\,(e_i)}{\mathrm{Re}\,(e_j)} \right|, \tag{2.10}$$

where e_i is an eigenvalue of the Jacobian matrix. Taking the identically zero eigenvalue as the denominator in Eq. (2.10) shows that the stiffness ratio r tends to infinity, provided that the real part of the numerator does not vanish. Stiffness of the considered autonomous system prevents the use of the Runge–Kutta-type solvers [62]—a feature that has been overlooked in some of the preceding studies.

2.4. Adams–Bashforth–Moulton solver

To integrate the stiff dynamical system, the variable-step-size predictor–corrector Adams–Bashforth–Moulton (ABM) method is employed [51,78]. This semi-implicit multistep scheme is particularly suitable for long-time simulations and stiff problems, offering improved efficiency and stability compared with explicit Runge–Kutta-type solvers [9,31,47,48].

2.4.1. Predictor (Adams–Bashforth, explicit step). The predictor stage of the ABM method is based on previously computed solution values. Consider the non-autonomous dynamical system (2.4), which, in finite-difference form, can be expressed as follows:

$$Y_{n+1} = Y_n + \frac{h}{2} \left(\sum_{k=1}^{N} a_k \left(G(Y_{n-k}) + F_{n-k} \right) \right), \tag{2.11}$$

where

$$Y_k = Y(\tau_k); \qquad F_k = F(\tau_k); \qquad h = \tau_{k+1} - \tau_k. \tag{2.12}$$

The integrating coefficients b_k depend upon the order N of the applied scheme [31]:

$$\begin{array}{c} N = 1: \quad a_1 = 1; \qquad N = 2: \quad a_1 = \frac{3}{2}; \quad a_2 = -\frac{1}{2} \\ N = 3: \quad a_1 = \frac{23}{12}; \quad a_2 = -\frac{16}{12}; \quad a_3 = \frac{5}{12} \end{array}. \tag{2.13}$$

2.4.2. Corrector (Adams–Moulton implicit step). The implicit corrector step of the considered ABM predictor–corrector scheme can be written in the following form [31]:

$$Y_{n+1} = Y_n + \frac{h}{2} \left(\sum_{k=0}^{N-1} b_k \left(G(Y_{n+1-k}) + F_{n+1-k} \right) \right), \tag{2.14}$$

where Y_{n+1} in the right-hand side is taken from predictor stage and the integrating coefficients b_k depend on the order N of the integrating scheme [31,43]:

$$\begin{array}{c} N = 1: \quad b_0 = \frac{1}{2}; \quad b_1 = \frac{1}{2}; \qquad N = 2: \quad b_0 = \frac{5}{12}; \quad b_1 = \frac{8}{2}; \quad b_2 = -\frac{1}{12} \\ N = 3: \quad b_0 = \frac{9}{24}; \quad b_1 = \frac{19}{24}; \quad b_2 = -\frac{5}{24}; \quad b_3 = \frac{1}{24} \end{array}. \tag{2.15}$$

Thus, taking into account Eqs. (2.13) and (2.15), the ABM third-order scheme is defined.

2.5. Cardinal number measure (CNM)

To define a cardinality measure, consider partitions of the corresponding projections [24]

$$\Delta x = \frac{x_{\max} - x_{\min}}{N}; \quad \Delta v = \frac{v_{\max} - v_{\min}}{N}, \tag{2.16}$$

where $x_{\max}; x_{\min}$ are the maximum and minimum values of the corresponding coordinate and N is the number of divisions along each axis, assumed equal for both coordinates.

For a point $(x, v) \in B$ on the attractor, the corresponding cell indices are computed as

$$i_x = \text{floor}\left(\frac{x - x_{\min}}{\Delta x}\right) + 1; \quad i_v = \text{floor}\left(\frac{v - v_{\min}}{\Delta v}\right) + 1, \tag{2.17}$$

with $1 \le i_x; i_v \le N$. This discretization scheme is commonly referred to as Ulam's method [70]. Now, the projection measures can be introduced:

$$C_x^* = \#\left\{c_x^i \mid (x) \in c_x^i \ \&\ (x, v) \in B\right\}; \quad C_v^* = \#\left\{c_v^i \mid (x) \in c_v^i \ \&\ (x, v) \in B\right\}, \tag{2.18}$$

where

$$c_x^i = [x_{\min} + (i_x - 1)\Delta x;\ x_{\min} + i_x \Delta x); \quad c_v^i = [v_{\min} + (i_v - 1)\Delta v;\ v_{\min} + i_v \Delta v). \tag{2.19}$$

The invariant projection measures are defined as

$$C_x = \frac{C_x^*}{N} \le 1; \quad C_v = \frac{C_v^*}{N} \le 1. \tag{2.20}$$

The fractal measures similar to (2.20) are also introduced in [25].

Taking the grid spacing set to $N = 100$ and following [24] small CNM, typically $C_{\max} < 0.25$, correspond to periodic motion. In particular, a period-n orbit is indicated, when $n \approx C_{\max} \times 100$, which reflects the fact that the largest Poincaré projection consists of a finite number of isolated points, each occupying a distinct grid cell. In this regime, the CNM provides a reliable and unambiguous indicator of periodicity, as the occupied cells are well separated. Larger values $0.25 < C_{\max} < 0.55$ usually correspond to quasi-periodic dynamics, which are associated with the appearance of attractors in the form of closed loops. In this case, the attractor appears as a smooth closed curve in the Poincaré section, corresponding to motion on a one-dimensional invariant torus. The CNM increases as the trajectory densely samples this curve, yet remains sufficiently low to preserve a clear geometric structure [24]. Chaotic dynamics with dense attractors occupying a large number of grid cells would correspond to higher values, typically $C_{\max} > 0.75$. In this regime, the Poincaré projection exhibits either a highly fragmented, cloud-like structure or an almost space-filling pattern, indicative of strongly irregular dynamics, leading to the occupation of a large number of grid cells. The high CNM values are therefore a signature of strongly chaotic behavior, as they reflect extensive phase-space exploration rather than localized geometric structures. Within the range $0.55 < C_{\max} < 0.75$, the system enters a transition region characterized by weak chaos. In this regime, the attractor progressively loses the smooth, loop-like structure associated with quasi-periodic motion, yet it does not fully develop the dense, space-filling patterns characteristic of strongly chaotic dynamics. Instead, the Poincaré projection exhibits partial fragmentation and intermittent clustering, reflecting the coexistence of regular and irregular dynamics.

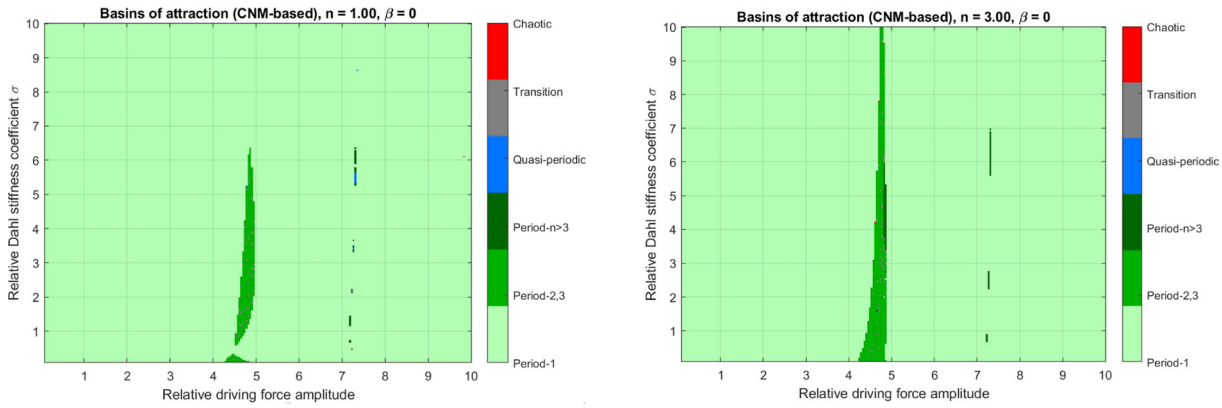


FIG. 4. Basins of attraction for $\beta = 0$: **a** $n = 1$; **b** $n = 3$

3. Numerical analysis

3.1. The model

Following [29,42,53,67], assume a moderately small dimensionless viscosity $\eta = 0.05$ to ensure weak damping conditions. This choice represents a practical compromise: It is small enough to preserve strong nonlinear interactions and complex dynamics, yet sufficiently large to ensure the formation of stable attractors and reasonable numerical convergence in long-time simulations. This choice of η is widely adopted in most works in structural dynamics [15,68,69]. The dimensionless linear stiffness coefficient $k = 1$ appearing in Eq. (1.1) is obtained after normalizing the equation of motion [42]. Accordingly, the dimensionless Coulomb friction coefficient is fixed at $F_c = 1$, placing the dry friction force on the same order of magnitude as the characteristic linear restoring force. The remaining key dimensionless parameters are varied over ranges:

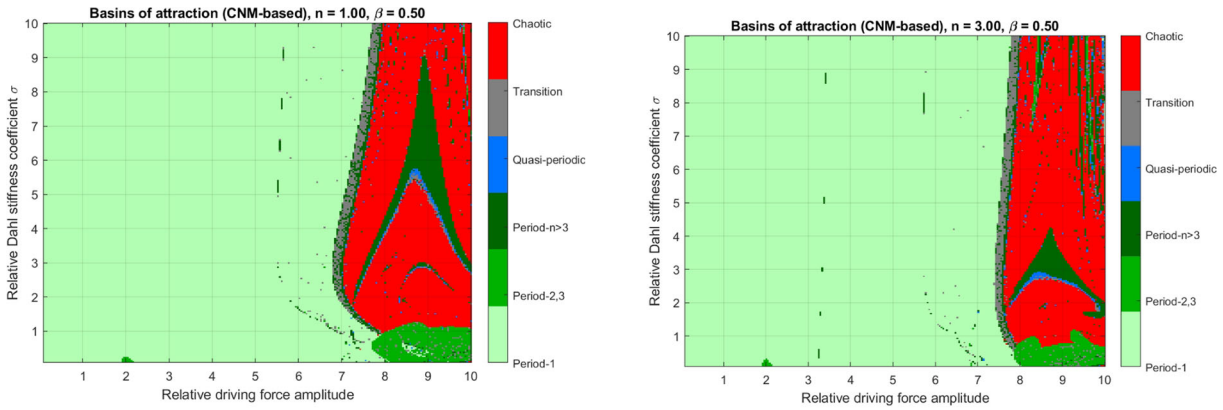
$$\beta \in [0;\ 2]; \qquad \sigma \in [0.1;\ 10]; \qquad f \in [0.1;\ 10]; \qquad n \in [1;\ 3]. \tag{3.1}$$

These intervals encompass regimes ranging from near-linear behavior at $\beta = 0$ low values of σ and f to strongly nonlinear, friction-dominated, and potentially chaotic dynamics at higher values of σ, allowing a comprehensive exploration of the system's bifurcation structure and response characteristics. Note also that considering only $\beta \geq 0$, materials exhibiting softening behavior are excluded.

According to the recommendations of [31], the ABM solver used in the present study is configured with the following parameters: Both predictor and corrector stages had equal number of steps $N = 3$. The basins of attraction were constructed using a method based on the cardinal number measure (CNM); see [19,76]. This approach quantifies the relative size of each basin by counting the proportion of initial conditions that converge to a given attractor, providing a straightforward and computationally efficient way to compare the dominance of coexisting attractors across the considered parameter sea.

3.2. Basins of attraction

3.2.1. Spring with linear response ($\beta = 0$). This case corresponds to a spring element with a linear response. The typical basins of attraction in the $(\sigma;\ f)$space for two values of the Dahl exponent, $n = 1$ and $n = 3$, are shown in Fig. 4.



(A) (B)

FIG. 5. Basins of attraction for $\beta = 0.5$: **a** $n = 1$; **b** $n = 3$

The plots in Fig. 4 reveal that in both cases, the system response is predominantly period-1. This behavior is consistent with the absence of spring nonlinearity, which suppresses the development of complex dynamical regimes. For $n = 1$ (Fig. 4a), a narrow region of a multiperiodic response emerges in a confined interval of the driving amplitude $4 < f < 5$. For $n = 3$ (Fig. 4b), the overall structure of the basins remains qualitatively similar, although the parameter region associated with period-n response becomes slightly more concentrated and vertically elongated. This suggests that increasing the Dahl exponent enhances sensitivity to variations in σ, while still preserving the dominance of regular periodic motion.

Overall, the results demonstrate that, in the absence of spring nonlinearity ($\beta = 0$), the system exhibits predominantly regular dynamics, with only localized transitions to more complex multiperiodic regimes. The influence of the Dahl exponent modifies the fine structure of the basins but does not fundamentally alter the global dynamical organization.

3.2.2. Weak cubic nonlinearity ($\beta = 0.5$). The typical basins of attraction for the considered case are shown in Fig. 5.

In contrast with the linear case ($\beta = 0$), the introduction of cubic spring nonlinearity significantly enriches the dynamical structure of the system. For $n = 1$ (Fig. 5a), a wide region of chaotic behavior emerges for larger values of the driving amplitude $f > 7$, as indicated by the extensive red areas. These chaotic domains are interwoven with regions of higher-period and quasi-periodic responses, forming intricate basin boundaries and suggesting strong sensitivity to parameter variations. Multistability is clearly observed, as different attractors coexist within overlapping parameter ranges, appearing as dark-green islands embedded in the surrounding red chaotic basin. For $n = 3$ (Fig. 5b), the global organization of the basins remains similar; however, the chaotic region becomes more vertically extended and concentrated to the left edge of the plot, indicating that increasing the Dahl exponent modifies the fine topology of the basins.

Overall, even a relatively small cubic nonlinearity ($\beta = 0.5$) drastically alters the system dynamics compared to the linear case. The response transitions from predominantly periodic motion to a complex mixture of periodic, quasi-periodic, and chaotic regimes, with pronounced multistability and intricate basin boundaries.

3.2.3. Strong cubic nonlinearity ($\beta = 2$). The typical basins of attraction for the considered case are shown in Fig. 6.

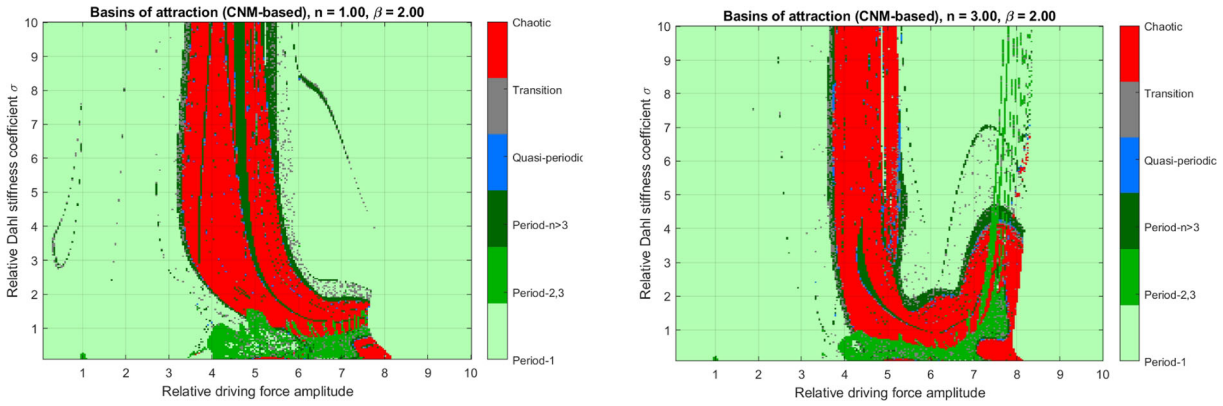


FIG. 6. Basins of attraction for $\beta = 2$: **a** $n = 1$; **b** $n = 3$

Compared with the previous cases ($\beta = 0$ and $\beta = 0.5$), the increase in cubic stiffness significantly intensifies the nonlinear effects and leads to a pronounced expansion of chaotic regions. For $n = 1$ (Fig. 6a), the chaotic regime dominates a broad interval of the driving amplitude $3.4 < f < 8.2$. The chaotic basin exhibits complex boundaries with embedded islands of higher-period solutions, indicating strong multistability and intricate transitions between regular and irregular motion. The deformation and bending of the chaotic region suggest the presence of successive bifurcations, possibly including period-doubling cascades and crisis phenomena. For $n = 3$ (Fig. 6b), the global structure remains qualitatively similar; however, the basins become more fragmented and structured. The coexistence of chaotic and higher-period attractors is more pronounced, and the parameter regions corresponding to periodic responses appear more localized and sharply bounded. This indicates that increasing the Dahl exponent enhances the sensitivity of the system to variations in both σ and f, modifying the topology of the attractor basins.

Overall, the results demonstrate that strong cubic nonlinearity ($\beta = 2$) leads to highly intricate chaotic dynamics in the physical parameter space, with extensive multistability and complex basin boundaries. The system behavior becomes markedly more irregular and parameter-sensitive compared with the weakly nonlinear and linear cases.

3.3. Bifurcation diagrams

To investigate transitions across various dynamical regimes, particularly the onset of intermittent chaos arising from the emergence of multiple isolated regions (or "spots") of periodic and quasi-periodic behavior embedded within the chaotic domain (Figs. 5 and 6), bifurcation diagrams are generated with the bifurcation parameter—driving force amplitude f. These diagrams are constructed using stroboscopic Poincaré sections of the long-term steady-state response: After discarding initial transients, the system's state is sampled once per forcing period to capture the discrete map of the attractor [24].

3.3.1. Weak cubic nonlinearity ($\beta = 0.5$). The typical bifurcation diagrams for the case ($\beta = 0.5$; $n = 1$; $\sigma = 2$), corresponding to basins of attraction presented in Fig. 5a, are shown in Fig. 7.

The plot in Fig. 7a shows that for small forcing amplitudes the system exhibits a single stable periodic orbit, manifested as a single branch in the bifurcation diagram ($f < 3.27$). In this regime, the response is synchronized with the external excitation, and the combined effect of the weak cubic nonlinearity $\beta = 0.5$ and moderately large friction force multiplier ($\sigma = 2$) does not yet induce qualitative changes in

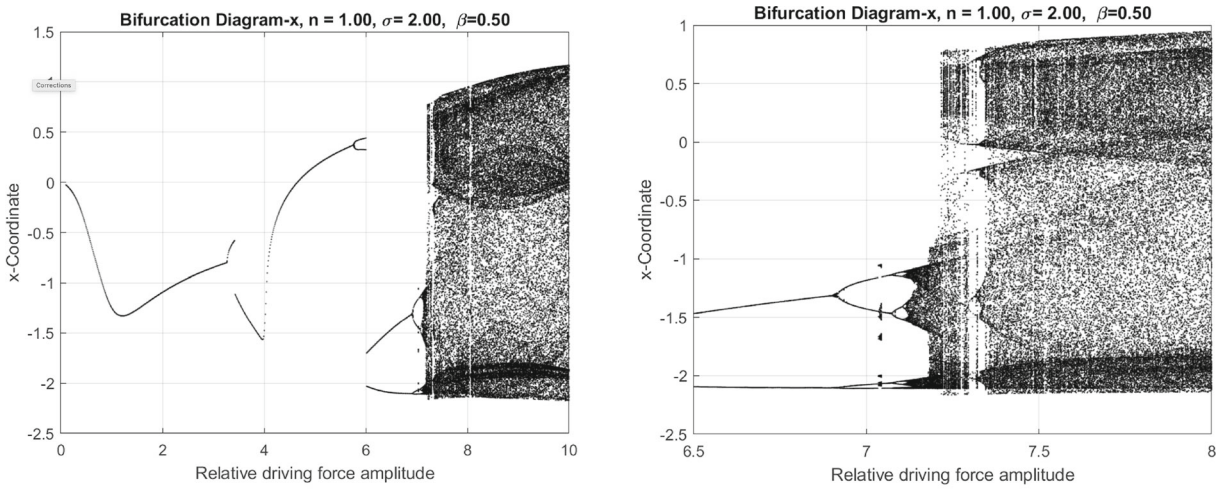


FIG. 7. Bifurcation diagrams in x-coordinate at $\beta = 0.5$; $n = 1$, and $\sigma = 2$: **a** the whole range $0.1 < f < 10$; **b** in the vicinity of transition region, $6.5 < f < 8$

the motion. As f increases, the interplay between the soft cubic nonlinearity and the hysteretic friction introduces branch splitting.

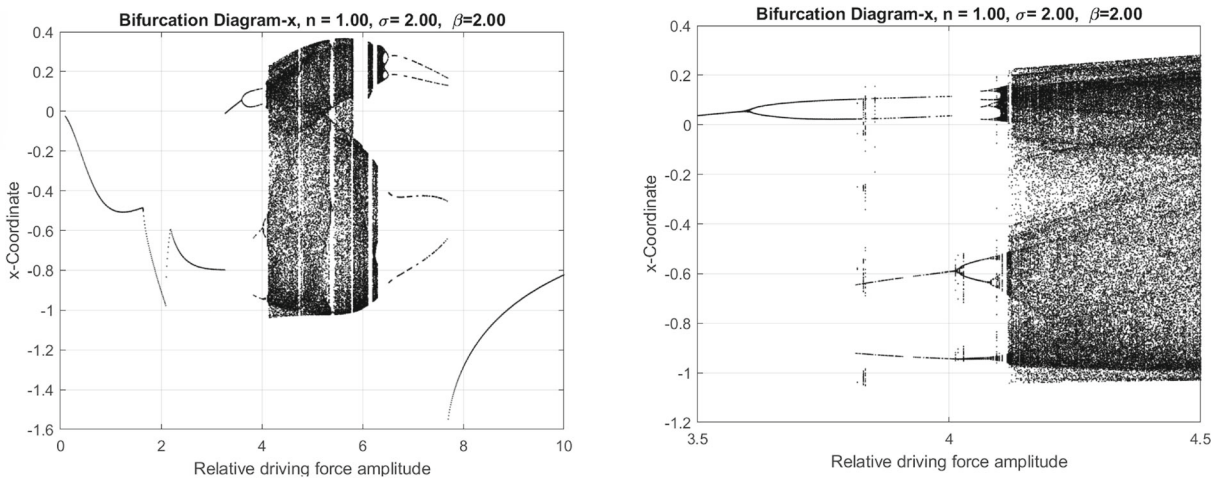
In the transition region ($6.5 < f < 7.5$), shown in Fig. 7b, a sequence of period-doubling bifurcations consistent with a Feigenbaum-type cascade emerge ($f \approx 6.7$–7.16). The diagram displays dense point clouds and banded structures, which signal the onset of intermittent dynamics and the transition to fully developed chaos. Within this chaotic domain, narrow periodic or quasi-periodic windows persist ($7.28 < f < 7.34$), reflecting temporary re-stabilization of the motion. The appearance of narrow periodic or multiperiodic windows within the chaotic regime, observed here apparently for the first time, is intrinsic to the considered combination of Duffing nonlinearity and the Bliman–Sorine friction model. In the classical Duffing oscillator without friction, such windows do not emerge [42].

3.3.2. Strong cubic nonlinearity ($\beta = 2$). The typical bifurcation diagrams for the case ($\beta = 2$; $n = 1$; $\sigma = 2$, corresponding to the basins of attraction shown in Fig. 6a, are presented in Fig. 8.

With a larger β, the restoring force becomes much stiffer at larger displacements, so the dynamics are shaped by a stronger competition between smooth cubic nonlinearity and the hysteretic, velocity-dependent friction. In the full-range plot (Fig. 8a), the system begins with a regular period-1 response at low forcing (up to $f \approx 3.5$), but the increased cubic stiffness causes earlier and sharper distortions of the orbit, leading to a rapid sequence of bifurcations as the forcing grows. The period-doubling cascade appears compressed compared to the weak-nonlinearity case, and the onset of chaos occurs at a lower forcing amplitude ($f > 4.11$). The zoomed-in panel around $3.5 < f < 4.5$ reveals a dense alternation of chaotic bands and narrow periodic windows, reflecting the sensitive interplay between the Duffing hardening effect and the non-smooth frictional hysteresis. The attractor structure becomes more fragmented.

4. Concluding remarks

In this study, the long-term dynamical behavior of a harmonically forced nonlinear oscillator incorporating Bliman–Sorine hysteresis spring element with varying degrees of nonlinearity is analyzed, controlled by the Dahl exponent n and friction stiffness coefficient σ, together with the cubic stiffness parameter β and



(A) (B)

FIG. 8. Bifurcation diagrams in x-coordinate at $\beta = 2$; $n = 1$, and $\sigma = 2$: **a** the whole range $0.1 < f < 10$; **b** in the vicinity of transition region, $3.5 < f < 4.5$

the forcing amplitude f. The basins of attraction in the (σ, f)-parameter space (relative friction stiffness coefficient vs. relative driving force amplitude) reveal a pronounced sensitivity to both the strength of the local restoring nonlinearity (via n) and the global cubic contribution (via β).

- In the linear response case ($\beta = 0$), the system remains predominantly in a period-1 regime for a wide range of parameters, with multiperiodic behavior emerging only at relatively high forcing amplitudes. These higher-order periodic responses appear within a narrow interval, approximately $4 < f < 5$, and their occurrence is largely insensitive to the value of the Dahl exponent n (Fig. 4).
- Introducing weak cubic nonlinearity ($\beta = 0.5$) enriches the dynamics: Chaotic regions (red in Fig. 5) emerge once the forcing amplitude becomes sufficiently large, typically for $f > 7$. These chaotic domains are interspersed with multiperiodic islands (dark green) for both low and high values of the Dahl exponent n.
- For strong cubic nonlinearity ($\beta = 2$), the interplay between cubic stiffening and hysteretic effects dominates, producing highly irregular basin topologies and causing chaotic regimes to appear at comparatively low forcing amplitudes, typically for $f > 3$ at $n = 1$ and for $f > 3.5$ at $n = 3$. The resulting basins become markedly more complex, with embedded periodic/quasi-periodic islands (Fig. 6).

The bifurcation diagrams (stroboscopic sections in the x-coordinate vs. driving amplitude f) confirm these observations and elucidate the routes to chaos:

- At $\beta = 0.5$, the diagrams show a classic Feigenbaum period-doubling cascade leading to chaos, with relatively broad chaotic bands at high f (Fig. 7).
- At $\beta = 2$, the transition occurs earlier and more abruptly: Period-1 motion destabilizes sooner, the doubling cascade compresses, and the chaotic attractor becomes larger and more fragmented, often interspersed with narrow periodic windows and evidence of crisis-like phenomena or intermittent chaos (Fig. 8).

Moreover, these regimes remain physically realizable for two reasons. First, the combined model of Duffing oscillator with friction is a generic model for a wide class of mechanical, electrical, and magneto-mechanical systems whose effective forcing frequency can be tuned over a broad range. Second, the chaotic attractors persist under systematic variation in the cubic stiffness and friction parameters, indicating

that the observed behavior is structurally stable rather than a consequence of fine-tuned or degenerate parameter choices.

These findings underscore the rich interplay between smooth cubic restoring forces and velocity-dependent hysteretic friction in shaping the system's vibrational response. The coexistence of periodic, multiperiodic, quasi-periodic, and chaotic regimes together with the pronounced sensitivity to forcing amplitude and frictional parameters suggests important implications for a wide range of engineering applications. Systems relying on frictional or hysteretic elements, such as vibration control devices, energy harvesters, and MEMS/NEMS actuators, may exhibit similar transitions between ordered and chaotic motion under harmonic excitation. Likewise, structures with nonlinear joints seismic bearings, and precision mechanisms affected by pre-sliding friction and frictional interfaces subjected to cyclic loading can benefit from the insights provided here, particularly regarding stability boundaries, multistability, and the onset of irregular dynamics.

It should also be noted that similar global analysis techniques have recently been applied to ship rolling dynamics modeled by Duffing-type and piecewise linear oscillators [21,22], where mixed-mode oscillations and crises were shown to create hidden risks of capsizing. Another remark refers to the observed ultra-low-frequency chaos and its structural stability is consistent with recent findings on chaotic ghosts in systems with slow parameter variation [64] where remnants of chaotic attractors cause delayed transitions and can be controlled by appropriate parameter reversal. The present observation of robust chaos at ultra-low driving frequencies suggests a possible underlying cause for such dangerous intermittent large-amplitude events in marine systems.

Author contributions SK involved in preparation of the main text. VB took part in editing the manuscript text and preparation of illustrations. All authors reviewed the manuscript.

Data Availability Statement No datasets were generated or analyzed during the current study.

Declarations

Conflict of interest The authors declare that they have no conflict of interest.

Open Access. This article is licensed under a Creative Commons Attribution 4.0 International License, which permits use, sharing, adaptation, distribution and reproduction in any medium or format, as long as you give appropriate credit to the original author(s) and the source, provide a link to the Creative Commons licence, and indicate if changes were made. The images or other third party material in this article are included in the article's Creative Commons licence, unless indicated otherwise in a credit line to the material. If material is not included in the article's Creative Commons licence and your intended use is not permitted by statutory regulation or exceeds the permitted use, you will need to obtain permission directly from the copyright holder. To view a copy of this licence, visit http://creativecommons.org/licenses/by/4.0/.

Publisher's Note Springer Nature remains neutral with regard to jurisdictional claims in published maps and institutional affiliations.

References

[1] Al-Bender, F., Swevers, J.: Characterization of friction force dynamics. IEEE Control Syst. Mag. **28**(6), 64–81 (2008)
[2] Al-Bender, F., Symens, W.: Dynamic characterization of hysteresis elements in mechanical systems. I. Theoretical analysis. Chaos **15**(1), 013105 (2005)
[3] Armstrong-Hélouvîy, B., Dupont, P., de Wit, C.C.: A survey of models, analysis tools and compensation methods for the control of machines with friction. Automatica **30**(7), 1083–1138 (1994)
[4] Awoyemi, D.O.: A p-stable liner multistep method for solving general third order initial value problems. Int. J. Comp. Math. **80**(8), 985–991 (2003)
[5] Balci, M.N.: Implementation of Dahl's dynamic friction model to contact mechanics of elastic solids. SN Appl. Sci. **3**, 92 (2021)

[6] Bliman, P.-A.: Mathematical study of the Dahl's friction model. Eur. J. Mech. A. Solids **11**(6), 835–848 (1992)
[7] Bliman, P.-A., Sorine, M.: Friction modelling by hysteresis operators. Application to Dahl, sticktion and Stribeck effects. In: Proceedings of Conference in Models of Hysteresis, Trento, Italy (1991)
[8] Bokobza, L.: Elastomer nanocomposites: effect of filler-matrix and filler–filler interactions. Polymers **15**(13), 2900 (2023)
[9] Bonchiş, C., Kaslik, E., Roşu, F.: HPC optimal parallel communication algorithm for the simulation of fractional-order systems. J. Supercomput. **75**, 1014–1025 (2019)
[10] Bouc, R.: Modèle mathématique d'hystérésis. Acustica **24**, 16–25 (1971)
[11] Bratov, V., et al.: Seismic barriers filled with solid elastic and granular materials: comparative analysis. Math. Mech. Solids **27**(9), 1761–1770 (2022)
[12] Brown, P., McPhee, J.: A continuous velocity-based friction model for dynamics and control with physically meaningful parameters. J. Comput. Nonlinear Dyn. **11**, 054502 (2016)
[13] Canudas de Wit, C., Olsson, H., Åström, K.J., Lischinsky, P.: A new model for control of systems with friction. IEEE Trans. Autom. Control **40**(3), 419–425 (1995)
[14] Chaturvedi, E., Mukherjee, J., Sandu, C.: A novel dynamic dry friction model for applications in mechanical dynamical systems. Proc. Inst. Mech. Eng. Part K J. Multi-body Dyn. **238**(1), 26–37 (2023)
[15] Chopra, A.K.: Dynamics of Structures: Theory and Applications to Earthquake Engineering, 4th edn. Prentice Hall (2012)
[16] Constantinou, M.C., Mokha, A., Reinhorn, A.M.: Teflon bearings in base isolation. II: Modeling. J. Struc. Eng. **116**(2), 455–474 (1990)
[17] Dahl, P.R.: A solid friction model, Aerospace Corporation Report AF04695-67-C-0158 (1968)
[18] Dahl, P.R.: Solid friction damping of mechanical vibrations. AIAA J. **14**, 1675–1682 (1976)
[19] Daza, A., et al.: Basin entropy: a new tool to analyze uncertainty in dynamical systems. Sci. Rep. **6**, 31416 (2016)
[20] Domínguez-Gurría, M.A., et al.: Dry friction energy dissipater with spherical elements. J. Vib. Eng. Technol. **12**, 8485–8494 (2024)
[21] Duan, J., et al.: Strange nonchaotic attractors in a class of quasi periodically forced piecewise smooth systems. Nonlin. Dyn. **112**, 1–13 (2024)
[22] Duan, J., et al.: Global dynamics and mixed-mode oscillations in nonlinear ship rolling with implications for capsizing. Ocean Eng. **341**, 122805 (2025)
[23] Dudchenko, A.V., et al.: Vertical wave barriers for vibration reduction. Arch. Appl. Mech. **91**, 257–276 (2021)
[24] Eckmann, J.-P., Ruelle, D.: Ergodic theory of chaos and strange attractors. Rev. Mod. Phys. **57**, 617–656 (1985)
[25] Frederickson, P., Kaplan, J., Yorke, E., Yorke, J.: The Lyapunov dimension of strange attractors. J. Diff. Eqs. **49**(2), 185–207 (1983)
[26] Friso, D.: A study of forced vibrations with nonlinear springs and dry friction: application to a mechanical oscillator with very large vibrating blades for soil cutting. Vibration **8**(1), 10 (2025)
[27] González-Carbajal, J., et al.: The role of dynamic friction in the appearance of periodic oscillations in mechanical systems. Nonlin. Dynam. **112**, 21587–21603 (2024)
[28] Grebogi, C., Ott, E., Yorke, J.A.: Crises, sudden changes in chaotic attractors, and transient chaos. Physica D **7**(1–3), 181–200 (1983)
[29] Guckenheimer, J., Holmes, P.: Nonlinear Oscillations, Dynamical Systems, and Bifurcations of Vector Fields. Springer, New York (1983)
[30] Guo, K., Jiang, J., Xu, Y.: Analyzing and characterizing the global complexity of bistable structures under simple harmonic excitation. J. Vib. Eng. Technol. **12**, 6401–6411 (2024)
[31] Hairer, E., Wanner, G.: Solving Ordinary Differential Equations II: Stiff and Differential-Algebraic Problems, 2nd edn. Springer, Berlin (1996)
[32] Han, N., et al.: Equilibrium states for a rotating mass-spring dry friction model on circular conveyor belt. Nonlinear Dyn. **113**, 34645–34676 (2025)
[33] Hartman, P.: Ordinary Differential Equations. Wiley, New York (1964)
[34] Heredia-Pérez, M., Alvarez, D.A., Bedoya-Ruiz, D.: A state-of-the-art review of the Bouc-Wen class model of hysteresis: origin, evolution and current state. Arch. Comput. Methods Eng. **33**, 1–51 (2026)
[35] Hong, H.-K., Liu, C.-S.: Coulomb friction oscillator: modelling and responses to harmonic loads and base excitations. J. Sound Vibr. **229**(5), 1171–1192 (2000)
[36] Il'yasov, K.K., et al.: Exterior 3D Lamb problem: harmonic load distributed over a surface. Mech. Solids **51**, 39–45 (2016)
[37] Johanastrom, K., Canudas-de-Wit, C.: Revisiting the LuGre friction model. IEEE Control Syst. Mag. **28**, 101–114 (2008)
[38] Keller, S., Fidlin, A.: Thermo-mechanical investigation of a friction oscillator under high-frequency excitation. Forsch. Ingenieurwes. **88**, 33 (2024)
[39] Kelly, J.M.: Earthquake-Resistant Design with Rubber. Springer, Berlin (1997)
[40] Kelly, J.M.: Analysis of fiber-reinforced elastomeric isolators. J. Seismol. Earthq. Eng. **1**(1), 19–34 (1999)

[41] Kelly, J.M.: Seismic isolation systems for developing countries. Earthq. Spectra **27**(2), 411–432 (2011)
[42] Kovacic, I., Brennan, M.J.: The Duffing equation: Nonlinear Oscillators and Their Behavior. Wiley, New York (2011)
[43] Kuznetsov, S.V.: Abnormal dispersion of Lamb waves in stratified media. Z. Angew. Math. Phys. **70**, 175 (2019)
[44] Kuznetsov, S.V.: Appearing ZGV point in the first flexural branch of Lamb waves in multilayered plates. Comp. Struct. **290**, 115532 (2022)
[45] Leniowski, R.: Modeling of torsional vibration in harmonic drives. Arch. Acoust. **32**(4), 923–931 (2007)
[46] Leus, M., Gutowski, P.: Analysis of longitudinal tangential contact vibration effect on friction force using Coulomb and Dahl models. J. Theor. Appl. Mech. **46**, 171–184 (2008)
[47] Li, S., et al.: Hybrid asynchronous absorbing layers based on Kosloff damping for seismic wave propagation in unbounded domains. Comput. Geotech. **109**, 69–81 (2019)
[48] Li, S., et al.: Benchmark for three-dimensional explicit asynchronous absorbing layers for ground wave propagation and wave barriers. Comp. Geotech. **131**, 103808 (2021)
[49] Luan, X., Zhu, Z.: Stochastic response of oscillators with fretting friction. J. Sound Vibr. **618**, 119353 (2025)
[50] Maegawa, S., Itoigawa, F.: Design method for suppressing stick-slip using dynamic vibration absorber. Tribol. Int. **140**, 1–8 (2019)
[51] Misirli, E., Gurefe, Y.: Multiplicative Adams Bashforth-Moulton methods. Numer. Algor. **57**, 425–439 (2011)
[52] Nagarajaiah, S., Sun, X.: Nonlinear dynamic analysis of base-isolated structures with elastomeric bearings exhibiting hardening behaviour. J. Eng. Mech. **127**(9), 1029–1036 (2001)
[53] Nayfeh, A.H., Mook, D.T.: Nonlinear Oscillations. Wiley, New York (1979)
[54] Olsson, H., et al.: Friction models and friction compensation. Eur. J. Control. **4**(3), 176–195 (1998)
[55] Pennestrì, E., Rossi, V., Salvini, P., Valentini, P.P.: Review and comparison of dry friction force models. Nonlin. Dyn. **83**(4), 1785–1801 (2016)
[56] Philips, J.R.: An integrated Stribeck friction model: analysis, simulation, and comparison with Dahl and LuGre. SIMULATION **101**(4), 477–491 (2025)
[57] Piatkowski, T.: Dahl and LuGre dynamic friction models—the analysis of selected properties. Mech. Mach. Theory **73**, 91–100 (2014)
[58] Polla, D., Owoloko, E.A.: Comparative analysis of Runge-Kutta-Fehlberg and Adams-Moulton methods for solving linear ordinary differential equations. Appl. Math. Sci. **7**(101), 5009–5018 (2013)
[59] Pontreau, M., Panëels, S., Bouchigny, S., Haliyo, S.: Design and evaluation of an active lubrication brake for a surgical drilling simulator. In: 2025 IEEE World Haptics Conference (WHC), pp. 1–14 (2025)
[60] Rice, J.R., Tse, S.T.: Dynamic motion of a single degree of freedom system following a rate and state dependent friction law. J. Geophys. Res. **91**, 521–530 (1986)
[61] Rizcallah, J.A.: Revisiting the coulomb-damped harmonic oscillator. Eur. J. Phys. **40**(5), 055004 (2019)
[62] Shampine, L.F., Gear, C.W.: A user's view of solving stiff ordinary differential equations. SIAM Rev. **21**(1), 1–17 (1979)
[63] Sreesha, R.B., Karthik, B.K., Shrikanth, V.: Krylov-Bogolyubov averaging based solution: nonlinear mode superposition in a 2-DOF system with Coulomb damping. J. Vib. Eng. Technol. **13**, 546 (2025)
[64] Su, H., et al.: Chaotic ghosts in systems with parameter drift: Delay and control critical transitions. Phys. Rev. E **113**, 044207 (2026)
[65] Swevers, J., Al-Bender, F., Ganseman, C., Projogo, T.: An integrated friction model structure with improved presliding behavior for accurate friction compensation. IEEE Trans. Automatic Control **45**(4), 675–686 (2000)
[66] Tutueva, A., Karimov, T., Butusov, D.: Semi-implicit and semi-explicit Adams-Bashforth-Moulton methods. Mathematics **8**(5), 780 (2020)
[67] Ueda, Y.: Randomly transitional phenomena in the system governed by Duffing's equation. J. Statist. Phys. **20**(2), 181–196 (1979)
[68] Ueda, Y.: Explosion of strange attractors exhibited by Duffing's equation. Ann. NY Acad. Sci. **357**, 422–434 (1980)
[69] Ueda, Y.: Random phenomena resulting from non-linearity in the system described by Duffing's equation. Int. J. Non-Linear Mech. **20**, 481–491 (1985)
[70] Ulam, S.M.: A Collection of Mathematical Problems. Interscience Publishers, New York (1960)
[71] Verma, P.K., Shrikanth, V.: A two-part analytical solution for the shock response spectrum with Coulomb damping. J. Vib. Eng. Technol. **12**(7), 7459–7470 (2024)
[72] Vitorino, M.V., Vieira, A., Rodrigues, M.S.: Effect of sliding friction in harmonic oscillators. Sci. Rep. **7**, 3726 (2017)
[73] Wang, Y., et al.: Rubber-filler interactions in carbon black-filled rubber composites studied by scanning transmission X-ray microscopy. J. Phys. Chem. B **129**(20), 5047–5053 (2025)
[74] Wen, Y.K.: Method for random vibration of hysteretic systems. J .Eng. Mech. Div. **102**(2), 249–263 (1976)
[75] Wiercigroch, M.: Comments on the study of a harmonically excited linear oscillator with a Coulomb damper. J. Sound Vibr. **167**(3), 560–563 (1993)
[76] Yang, J., et al.: Vibrational resonance in coupled self-learning Duffing oscillators and its application in noisy radio frequency signal processing. Phys. Lett. A **571**, 131311 (2026)

[77] Zhang, B., et al.: Dahl friction model for driving characteristics of V-shape linear ultrasonic motors. Micromachines **13**(9), 1407 (2022)
[78] Zhao, B., Zhang, B.: Comparison of different order Adams-Bashforth methods in an atmospheric general circulation model. Acta Meteorol. Sin. **25**, 754–764 (2011)

Vladimir Bratov
Edinburgh Napier University
Edinburgh
UK
e-mail: v.bratov@napier.ac.uk

Sergey V. Kuznetsov
Moscow State University of Civil Engineering
Moscow
Russia
e-mail: kuzn-sergey@yandex.ru

(Received: April 3, 2026; revised: May 13, 2026; accepted: May 18, 2026)